Hall2De numerical simulations for the assessment of pole erosion in a magnetically shielded Hall thruster

IEPC-2015-249／ISTS-2015-b-249

Presented at Joint Conference of 30th International Symposium on Space Technology and Science
34th International Electric Propulsion Conference and 6th Nano-satellite Symposium,
Hyogo-Kobe, Japan
July 4 – 10, 2015

Alejandro Lopez Ortega[1], Ioannis G. Mikellides[2] and Ira Katz[3]
Jet Propulsion Laboratory, California Institute of Technology, Pasadena, CA, 91109, United States

Abstract: Magnetic shielding of Hall thrusters has been shown to reduce erosion of the channel walls by at least a few orders of magnitude thereby enabling the use of these devices in deep space missions. Recently, a 150-hour wear test of a magnetically shielded laboratory Hall thruster (H6MS) operating at 300V and 6kW revealed unexpected sputtering of the inner pole surface. In this paper we present results from numerical simulations with Hall2De aimed at understanding the cause(s) of the erosion measured at the inner pole. Hall2De is a 2-D axisymmetric code that makes use of a hydrodynamics formulation for both electrons and ions and assumes a quasi-neutral plasma. A space charge algorithm, which provides a correction of the plasma potential in regions where these approximations fail, has been included in order to reproduce the correct features of the electric field in the vicinity of the poles. We employ a computational domain that emulates closely the geometry of the thruster, even replicating a gap between the inner pole and the acceleration channel. This first study reveals that erosion rates inferred from the plasma conditions produced in Hall2De simulations under-predict the measured values by factors of 3 to 15. An investigation of possible causes for the observed erosion rates in the wear test follows, focusing on the influence of beam ions and possible oscillations in the plume. Numerical results suggest that beam ions are an unlikely cause for erosion. For beam ions to bombard the pole surface at sufficient rates, the acceleration region must be located far downstream of its experimentally determined position. In addition, the high amplitude of the discharge oscillations that would be required to replicate the erosion measurements contradict the time-resolved measured performance. Finally, it is found that large oscillations induced by the cathode flow are required in order to explain the erosion rates reported at the wear test. The dynamical behavior of the plasma in the vicinity of the inner pole is the subject of a near-term experimental campaign.

Nomenclature

α	=	proportionality parameter for high-frequency oscillations in the vicinity of the cathode
$\mathbf{B}$	=	magnetic field
β	=	incidence angle of ions on pole surfaces
C	=	carbon
Δt	=	time-step (in numerical simulation)
Δz	=	magnitude of axial shift of the anomalous collision frequency profile

[1]Member of the Technical Staff, Electric Propulsion Group, 4800 Oak Grove Drive, Pasadena, CA, 91109, Mail Stop 125-109
[2]Principal Engineer, Electric Propulsion Group, 4800 Oak Grove Drive, Pasadena, CA, 91109, Mail Stop 125-109
[3]Group Supervisor, Electric Propulsion Group, 4800 Oak Grove Drive, Pasadena, CA, 91109, Mail Stop 125-109

ε	=	erosion rate (in mm/hr unless otherwise specified)
ε_0	=	vacuum permittivity
f_β	=	angle-dependent part of sputtering yield
f_k	=	energy-dependent part of sputtering yield
$\mathbf{j}$	=	current density vector
K	=	ion energy in sputtering yield computations (in eV)
L	=	length of the acceleration channel
m	=	particle mass
Mo	=	molybdenum
n	=	density field
p	=	pressure field
ϕ	=	plasma potential
q	=	particle charge
r	=	radial coordinate
$\mathbf{R}$	=	drag vector
R_c	=	outer radius of carbon cover of the inner pole
$R_{midchannel}$	=	distance from channel centerline to thruster centerline
t	=	time (in numerical simulation)
t_c	=	thickness of carbon cover of the inner pole
T	=	temperature (in eV)
τ	=	period of oscillations
$\mathbf{u}$	=	velocity field
Y	=	sputtering yield (in mm^3/C unless otherwise specified)
z	=	axial coordinate
e	=	(subscript) electron property
F	=	(subscript) result of solving fluid equations in Hall2De
k	=	(subscript) cell number (in numerical simulation)
iF	=	(subscript) ion population in multi-fluid simulations
iz	=	(subscript) charge state of ions
SC	=	(subscript) result of solving space charge algorithm in Hall2De
$wall$	=	(subscript) denotes conditions at physical boundaries
0	=	(subscript) denotes conditions at the sheath edge
//	=	(subscript) direction parallel to magnetic field lines

I. Introduction

Hall effect accelerators have been identified over the last decade as potential candidates for application of solar electric propulsion to deep space missions. For instance, the proposed Asteroid Redirect Mission (ARM), which plans to robotically capture a small near-Earth asteroid and redirect it safely to a stable orbit in the Earth-moon system [1], would require Hall thrusters operating at a specific impulse (I_{sp}) of ~3000 s. (~800 V) [2-3] with an estimated throughput of 12,000 kg of xenon [3] over more than 20000 hours of operation.

In the past, the life expectancy of Hall thrusters was mainly limited by the erosion of the acceleration channel walls, which inevitably leads to exposure of critical magnetic circuit components to the plasma. One technique that has been shown to overcome this limitation has been termed "magnetic shielding" [4] and, acknowledging that the main cause of erosion in the discharge channel is the existence of plasma potential gradients and high electron temperatures that drive energetic ions towards the walls, proposes a design strategy for the magnetic field topology that avoids such conditions. In a succinct manner, a change in the topology of the magnetic field lines is sought such that they "graze" the channel walls instead of meeting them at an angle. It is well-known that the lines of force in the Hall thruster channel are also isothermal lines, resulting in a potential distribution along them that closely follows the Boltzmann relation for electrons. By enforcing an electron temperature as cold as possible along the grazing lines, the plasma potential along the channel walls remains approximately constant, which in turn, precludes the acceleration of ions towards the walls. The principles of magnetic shielding were inspired by numerical simulations with the Hall2De code [5]. A proof-of-concept investigation of the magnetic shielding principles was conducted at

Fig. 1. Left: H6MS thruster before wear testing. The acceleration channel rings appear white and no surface roughening of the inner pole surface is evident. Right: The H6MS after a 150-h wear test in a JPL facility at 300 V and 20 A. The channel rings appear dark as the reduced erosion rates fell well below the deposition rates, allowing for build-up of carbon onto the ring surfaces. Roughening of the inner and outer pole surfaces became evident suggesting some sputtering could have occurred.

the Jet Propulsion Laboratory in 2010-2012 [4,6,7] and involved the modification of 6 kW-class laboratory Hall thruster called H6 [8] from its original configuration, hereinafter termed H6US, to a magnetically shielded one (H6MS) with the guidance of Hall2De simulations. A 150-hour wear test of the latter at nominal conditions (300V, 20A) revealed that erosion rates at the channel walls were 2 to 3 orders of magnitude lower than those found in the H6US. These measured rates were in agreement with the numerical simulation predictions. More recently, numerical simulations of the H6MS were performed for the discharge voltage range of 400-700 V at constant power (6 kW) and at 800 V, 9 kW [9]. The simulations were followed by performance and wear testing at the 800 V, 9 kW operating condition [10]. The combination of simulations and tests showed that the effectiveness of magnetic shielding to reduce channel erosion by at least a few orders of magnitude was retained at higher discharge voltages so long as the magnetic circuit was capable of supplying the intended magnetic field topology [9].

While mitigation of the channel erosion was demonstrated in the 150-hour wear test, a post-test visual inspection revealed roughening of the inner and outer pole surfaces. Figure 1 shows photographs of the H6MS before (left) and after (right) the 150-h wear test at 300 V-6 kW, where the changes in the appearance of the pole surface can be clearly observed, along with darkening of the insulator rings (originally of white color) caused by carbon deposition from the test facility. The evidence of ion sputtering at the inner pole during the test, contrasted with the results of preliminary Hall2De simulations [11] that yielded negligible erosion rates along this surface, motivated a second 150-hour wear test focused on quantitatively evaluating the erosion rates at the poles. This test was conducted in the fall of 2014, with the results of that campaign being presented in a companion paper [12] and summarized here for completion. The tested thruster had installed a carbon cover with thickness t_c/L=0.08 and outer radius $R_c/R_{midchannel}$ =0.619 to protect the magnetic material. The addition of the cover moves the exposed surface 0.03L axially downstream of the acceleration channel exit. Samples of molybdenum were also placed on the surface to allow for the extraction of the average ion energy and current density from the comparison of the erosion rate ratio between carbon and molybdenum. Figure 2 depicts the measured erosion rate on carbon and molybdenum as a function of radial position as well as the average values. At the outer pole, erosion was only observed in the region immediately adjacent to its inner diameter and its rate was very low compared to the values measured at the inner pole. Even when the erosion is slightly more acute near the pole edges, differences between minimum and maximum radial values for each material remain within an order of magnitude. These results also suggest that a 3.5mm-thick carbon cover will protect the poles sufficiently to allow for over 50000 hours of operation. Making use of the ratio of average erosion rates and the available experimental data for the sputtering yield of molybdenum [13-15] and carbon [13-18], the average energy of ions impacting the pole walls is predicted to be large, in the vicinity of 130V (with a lower bound due to uncertainties in measurements and models of 80V), with the ion current density being 7A/m^2. These results only account for perpendicular bombardment of singly charged ions.

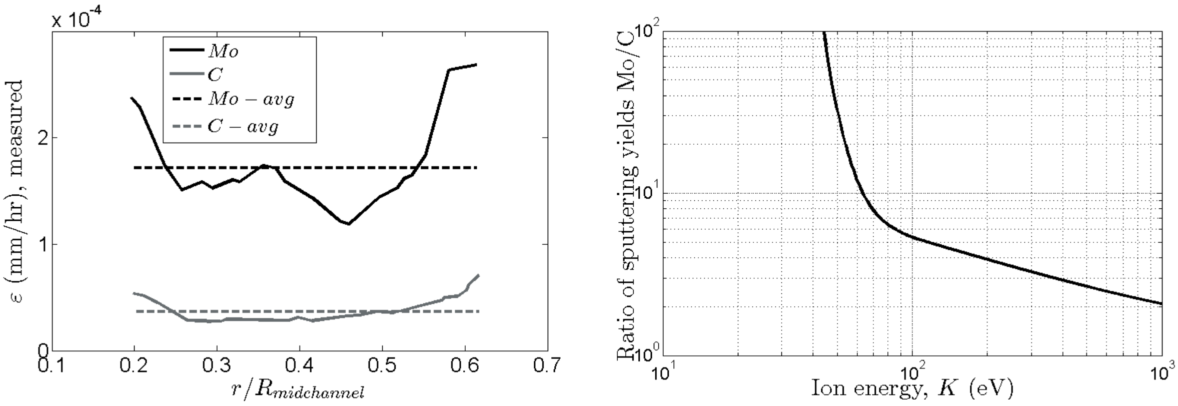

Fig. 2. Left: Measured erosion rates in mm/hr in the carbon cover and molybdenum samples along the inner pole surface (referenced to the radial location of the channel centerline with respect to the thruster centerline). Average values (C=3x10^{-5} mm/hr, Mo=1.5x10^{-4} mm/hr) used to make a first estimation of the mean energy of ions impacting the walls are marked with dashed lines. Right: Ratio of C and Mo sputtering yields (see section IIc for further detail). A ratio of ~5 is achieved for K~130eV.

The objective of the work reported in this paper is to identify possible source(s) of high energy ion bombardment of the inner pole by means of Hall2De numerical simulations. The possibility of sputtering of the outer pole is not analyzed here as experimental evidence indicates that this phenomenon is restricted to a very narrow region close to the channel exit and the rate of erosion there is lower (by at least an order of magnitude) than that reported for the inner pole. Section II provides a description of Hal2De focusing on recent and relevant advancements made in the code. A key improvement in the algorithm, specifically aimed at producing an accurate topology of the plasma properties in the vicinity of the chamfered channel walls, is a space-charge algorithm that produces a solution for the plasma potential in regions of low density where the plasma quasi-neutrality assumption fails. Also included in this section is a description of the sputtering yield models employed for carbon and molybdenum. Section III explores the erosion rates at the inner pole derived from the steady state computational solution when the exact thruster geometry has been implemented and the space charge algorithm introduced in Section II has been employed. In Section IV, we explore the possibility of beam oscillations not captured in the numerical model being responsible for the ion bombardment. In Section V, the possible impact of cathode-related oscillations on the erosion of the poles is investigated. Concluding remarks are provided in Section VI.

II. Computational method and sputtering yield models

A. General description of Hall2De

Hall2De is a numerical code for the simulation of the plasma discharge in Hall effect accelerators that has been developed at the Jet Propulsion Laboratory over the last decade. Its most notable features are described here whilst the interested reader can find the specifics of the numerical implementation in [5]. In Hall2De, a quadrilateral-based computational grid aligned with the magnetic field is employed. A typical simulation domain comprises the acceleration channel and a region of the plume that extends several times the length of the channel in the radial and axial directions. The dimensions of the computational domain enable a realistic simulation of the cathode plume (but not the hollow cathode interior). Cylindrical geometry is assumed, with the axis being the thruster centerline, in a way such that equations of motion are only solved in the axial and radial directions. This simplification is particularly beneficial in the case of internally mounted cathodes but requires certain approximations to be made when configurations with external cathodes are simulated. The motion of each of the species in the plasma is solved separately. The density and velocity distribution of neutral particles is modeled using free-molecular flow, according to the view-factor algorithm described in [19]. Ions are modeled using a hydrodynamic approach where they are divided into multiple populations, *iF*. Typically two populations are sufficient: ions with high and low energy, generated upstream and downstream of the acceleration region, respectively. Separate continuity and momentum equations are solved for each population and each charge state, *iZ*. Ions of different *iF* and *iZ* numbers can interact with one another through ionization, charge exchange, and elastic collisions. The distinction between populations of high and low energy ions was introduced in the numerical code after establishing that collisions in the plume region are typically scarce enough such that beam and plume ions are not necessarily in equilibrium with one another. Attempting to solve all the ions with a single set of equations would result in reduced values of plasma density in the plume, as can be inferred from a continuity argument where the large velocity of the beam ions dominates over the low speeds of ions generated downstream of the acceleration region. The effect of using multiple ion populations over a single population was quantified in [20]. Since under-predicting the concentration of ions in the pole regions can result in reduced erosion rates, all the simulations featured in this article use the two-population approach. The threshold between the two is established by the maximum kinetic energy that an ion generated at a particular location would achieve, which can be approximated by the plasma potential, rather than geometry. In the simulations reported in this article, the threshold between the two populations is set at 75V, with sensitivity tests showing that the threshold value has little influence in the erosion predictions in the range spanning from 50 to 150V. Finally, electron motion is modeled using a fluid approach where inertia is neglected. This approach results in a vector form of Ohm's law that is solved in the directions parallel and perpendicular to the magnetic field lines and enables computation of the plasma potential when combined with current conservation and the assumption of plasma quasi-neutrality. Electron temperature is determined as the solution of an energy conservation equation [5].

B. Space charge algorithm

The approach described above is valid in the vast majority of the computational domain. However, the fluid approximation employed for ions and electrons fails in regions of low plasma density close to the thruster walls. As shown in Fig. 3, the vicinity of the chamfered region of the acceleration channel, typical of magnetically shielded configurations, is prone to low density conditions due to the combination of the chamfered geometry with electric fields that accelerate ions in the axial direction. Attending at the Debye length in those regions, the width of the sheath can be comparable to (or even larger than) the typical cell size. This phenomenon results in two issues: the plasma potential cannot be determined accurately in this region from a fluid approximation that assumes quasi-neutrality, and the boundary conditions, which assume a thin sheath when compared to the typical cell dimensions, cannot be applied. As it was argued in [11,21], since the motion of ions is determined to great extent by the resulting electric field, inaccuracies in the topology of the latter due to the assumptions made in the code can potentially result in unrealistic ion trajectories that alter the predicted erosion rates. In order to circumvent these difficulties and produce more accurate predictions of ion bombardment to the pole surfaces, we included in Hall2De a space charge algorithm that uses the underlying information of the solution of the fluid equations to produce a modified plasma potential in regions where plasma quasi-neutrality is not satisfied.

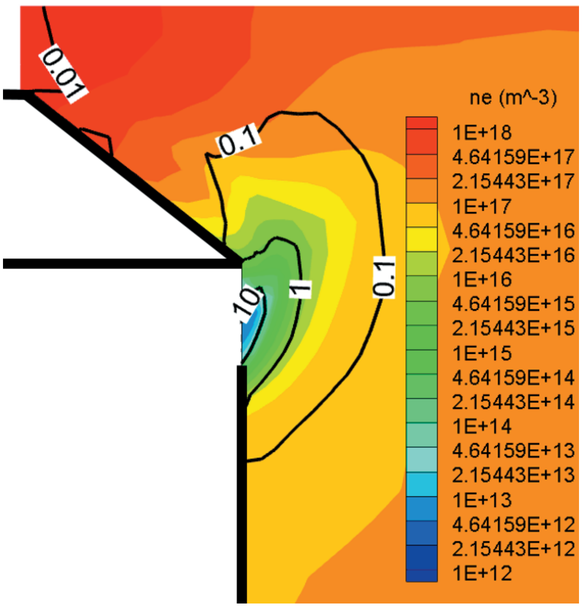

Fig. 3. Color: plasma density contours in the vicinity of the chamfered region of the acceleration channel, inner wall. Similar density contours are found in the outer channel wall. Lines: ratio of Debye length with respect to characteristic cell length (square root of the cell area in the z-r plane).

The space charge algorithm is implemented as follows. At each computational time-step, the solutions for neutral particles, ion density and momentum, electron temperature, and plasma potential are evolved according to the hydrodynamics equations described in [5,20]. At the end of the time step, regions close to the thruster walls where the sheath is finite compared to the cell size are identified and a new solution of the plasma potential is obtained in those cells by use of the space charge algorithm. The flagging criterion is the local Debye length being comparable to the distance from the cell centroid to the nearest wall. A threshold for the exact value of the ratio between the latter two variables to trigger the space charge algorithm was implemented to explore the sensitivity of the solution. Test showed that results remain independent of the chosen threshold value, as the space charge potential converges to the fluid solution in regions of high density. Finally, the modified plasma potential is employed to compute the electric field spatial distribution that is employed in the following time step to determine the ion momentum, according to

$$\frac{\partial\left(n_{iz,iF}\mathbf{u}_{iz,iF}\right)}{\partial t}+\nabla\cdot\left(n_{iz,iF}\mathbf{u}_{iz,iF}\mathbf{u}_{iz,iF}+\frac{p_{iz,iF}}{m_{Xe}}\mathbf{I}\right)=-q_{iz,iF}\nabla\phi_{sc}+\mathbf{R}_{iz,iF}. \tag{1}$$

In regions where the space charge algorithm is enforced, Poisson's equation is solved to determine the space charge potential as follows:

$$\nabla^2\phi_{SC}(\mathbf{x},t)=-\frac{q_e}{\varepsilon_0}\left(n_{e,F}(\mathbf{x},t)-n_{e,SC}(\mathbf{x},t)\right). \tag{2}$$

The first term on the right-hand side represents the quasi-neutral plasma density and can be recovered from the solution of the fluid equations as the summation of the density of all ion species,

$$n_{e.F}=\frac{1}{q_e}\sum_{iz}\sum_{iF}q_{iz,iF}n_{iz,iF}. \tag{3}$$

In order to determine $n_{e,SC}$, it is necessary to make some assumptions about the distribution function followed by the electron population in the sheath. We assume a Maxwellian distribution of the form

$$n_{e,SC}(\mathbf{x},t)=n_{e,0}\exp\left(\frac{\phi_{SC}(\mathbf{x},t)-\phi_0}{T_{e,0}}\right), \tag{4}$$

where $n_{e,0}$ and ϕ_0 are a pair of values of the plasma density and potential, respectively, at the edge of the sheath when an isothermal line is followed from the point at which $n_{e,SC}$ is being evaluated. We can take advantage of some of the known properties of magnetized electrons along B-lines to determine the values of $n_{e,0}$, ϕ_0, and $T_{e,0}$ in a simple way. It is well-known that magnetic field lines in Hall thrusters are isothermal in the vicinity of the acceleration region [4]. In addition, along magnetic field lines, Ohm's law may be expressed as

$$E_{//}=\eta j_{e,//}-\frac{T_e}{n_e}\nabla_{//}n_e. \tag{5}$$

The electron current term can be neglected since the resistivity along magnetic field lines is very low. Hence, the fluid approximation along magnetic field lines resembles the Boltzmann relation for electrons and the unknown values at the edge of the sheath can be related for convenience to the fluid values of the plasma density and potential in the location at which the space charge potential is being evaluated,

$$n_{e,F}(\mathbf{x},t)=n_{e,0}\exp\left(\frac{\phi_F(\mathbf{x},t)-\phi_0}{T_{e,F}(\mathbf{x},t)}\right). \tag{6}$$

Combining the latter expression with Eq. (4), the space charge density finally yields,

$$n_{e,SC}(\mathbf{x},t)=n_{e,F}(\mathbf{x},t)\exp\left(\frac{\phi_{SC}(\mathbf{x},t)-\phi_F(\mathbf{x},t)}{T_e(\mathbf{x},t)}\right). \tag{7}$$

Numerical tests performed using this assumed distribution function for the electrons led to non-monotone values of the plasma potential in the sheath (for instance, negative values of the plasma potential when the walls are grounded). This is because the distribution function does not take into account that such a solution of the plasma potential will ultimately deplete the sheath of all the electrons with lower energies than the wall potential. To address this difficulty, we implemented a truncated Maxwellian distribution in which no electrons whose energy is lower than the minimum wall potential at the boundaries of computational domain are allowed:

$$n_{e,SC}(\mathbf{x},t)=n_{e,F}(\mathbf{x},t)\left[\exp\left(\frac{\phi_{SC}(\mathbf{x},t)-\phi_F(\mathbf{x},t)}{T_e(\mathbf{x},t)}\right)-\exp\left(\frac{\min(\phi_{wall})-\phi_F(\mathbf{x},t)}{T_e(\mathbf{x},t)}\right)\right]. \tag{8}$$

Boundary conditions are required to numerically solve the differential equation (2). The first type of boundary conditions relate the space charge solution of the potential with the fluid solution. This can be achieved simply by enforcing that for all the cells for which the space charge potential is not required, $\phi_{SC} = \phi_F$. The second type of boundary condition is of the Dirichlet type and it is enforced at the wall boundaries. For conductor materials, the boundary potential is specified. In the case of an insulator material, the wall potential is determined by invoking the zero-current boundary condition at the wall,

$$\sum_{iz}\sum_{iF} \mathbf{j}_{iz,iF} \cdot \hat{\mathbf{n}} = -\mathbf{j}_e \cdot \hat{\mathbf{n}} = q_e n_{e,F} \sqrt{\frac{q_e T_e}{2\pi m_e}} \left[\exp\left(\frac{\phi_{wall} - \phi_F}{T_e} \right) - \exp\left(\frac{\min\left(\phi_{wall}^t\right) - \phi_F}{T_e} \right) \right], \tag{9}$$

where the fluid variables at the cell immediately adjacent to the each boundary edge are used. Since the minimum value of the wall potential cannot be determined until Eq. (9) has been evaluated at all the boundary edges, the truncation term of the Maxwellian distribution makes use of the last known value of the minimum wall potential (the value at the previous time-step).

The resulting equation is solved at each cell centroid using an implicit-linearized approach. The fully implicit system of equations that determines the plasma potential at each cell k reads

$$\nabla_k^2 \phi_{SC}^{t+\Delta t} = -\frac{q_e n_{e,F,k}}{\varepsilon_0} \left[1 - \exp\left(\frac{\phi_{SC,k}^{t+\Delta t} - \phi_{F,k}}{T_{e,k}} \right) + \exp\left(\frac{\min\left(\phi_{wall}\right) - \phi_{F,k}}{T_{e,k}} \right) \right], \tag{10}$$

where the discretized linear Laplacian operator ∇_k^2 is the same used in other equations implemented in Hall2De [5], and is subject to the aforementioned Dirichlet boundary conditions at the external boundaries. Here we have omitted the temporal superscripts for the variables that are determined in the solution of the fluid equations. This system of equations is non-linear and requires an iterative process, such as Newton-Raphson, to be solved. A Taylor series linearization of the exponential term centered at the solution of the previous time-step,

$$\exp\left(\frac{\phi_{SC,k}^{t+\Delta t} - \phi_{F,k}}{T_{e,k}} \right) \approx \exp\left(\frac{\phi_{SC,k}^{t} - \phi_{F,k}}{T_{e,k}} \right) + \frac{\left(\phi_{SC,k}^{t+\Delta t} - \phi_{SC,k}^{t}\right)}{T_{e,k}} \exp\left(\frac{\phi_{SC,k}^{t} - \phi_{F,k}}{T_{e,k}} \right), \tag{11}$$

allows us to transform the system of equations (10) so it can be solved without iterations:

$$\begin{aligned} &\nabla_k^2 \phi_{SC}^{t+\Delta t} - \frac{q_e n_{e,F,k}}{\varepsilon_0} \exp\left(\frac{\phi_{SC,k}^{t} - \phi_{F,k}}{T_{e,k}} \right) \phi_{SC,k}^{t+\Delta t} = \\ &= -\frac{q_e n_{e,F,k}}{\varepsilon_0} \left[1 - \exp\left(\frac{\phi_{SC,k}^{t} - \phi_{F,k}}{T_{e,k}} \right) \left(1 - \frac{\phi_{SC,k}^{t}}{T_{e,k}} \right) + \exp\left(\frac{\min\left(\phi_{wall}\right) - \phi_{F,k}}{T_{e,k}} \right) \right]. \end{aligned} \tag{12}$$

To illustrate the effect of implementing this algorithm, we depict in Fig. 4 the plasma potential and ion density contours of singly charged beam and plume ions in a region close to the channel exit with and without the use of the space charge algorithm. Ion velocity vectors are also shown. In this simplified example, the actual geometry of the poles has not been modeled (see Fig. 6 in the following section) and flat vertical surfaces located at the channel exit plane have been employed instead. In order to illustrate the effect of having both insulator and boundary conditions, they have been applied to the outer and inner poles, respectively. We observe changes in the plasma potential topology in the regions of low density identified in Fig. 3. The ~300V contour, which in the fully-hydrodynamic simulation ended at the pole surfaces is now restricted by the boundary conditions. At the inner pole, the 0V boundary condition forces the plasma contours to become more rounded and not to extend radially as far as in the fully-hydrodynamic solution of the potential. This results in a higher radial component of the electric field that accelerates ions towards the pole region. We also observe that the density of beam ions in the region between the main beam and the cathode plume has increased by an order of magnitude. This change in the potential also has an effect on plume ions. In the fluid simulation, the inaccurately large gradient of the plasma potential close to the outer

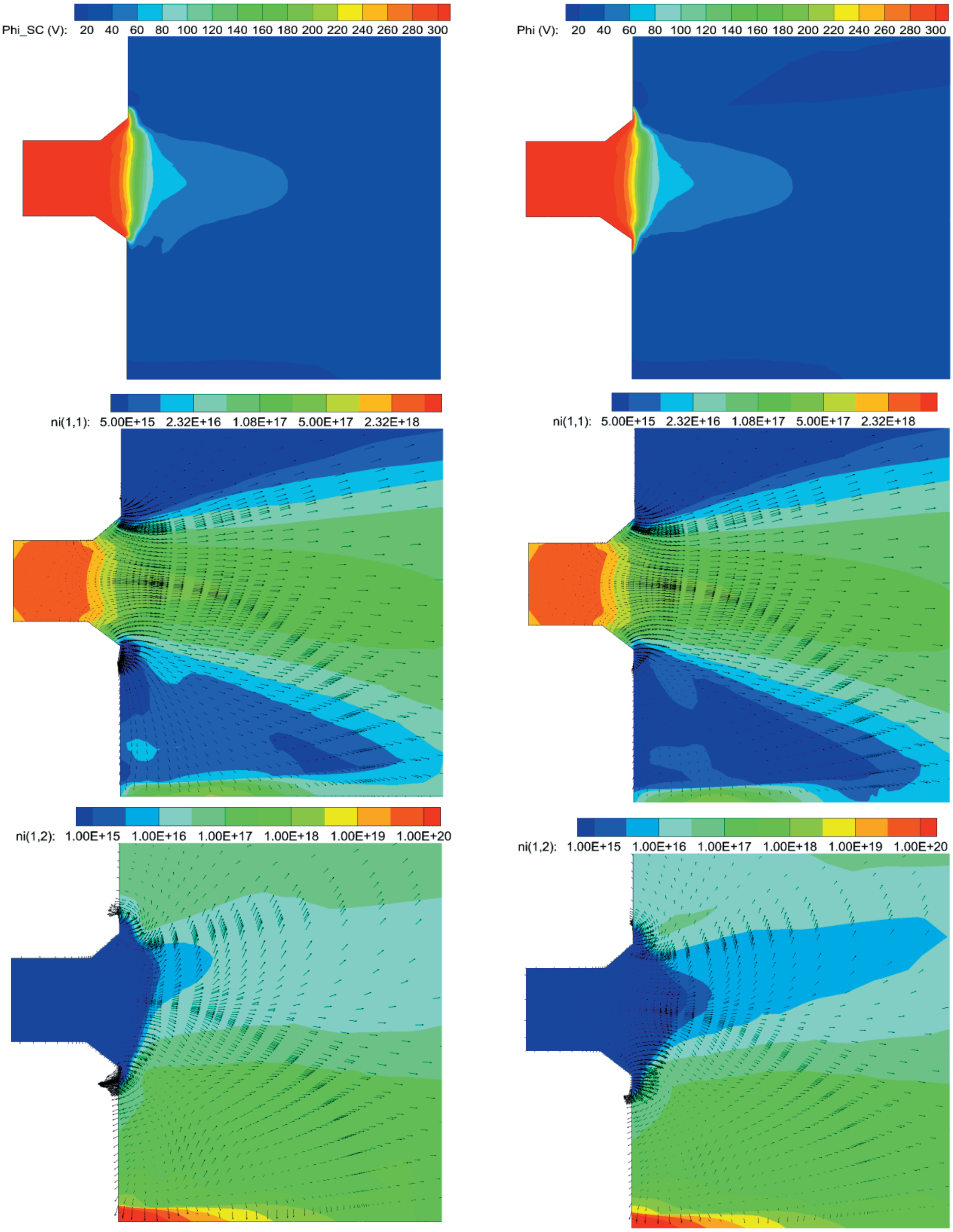

Fig. 4. Plasma potential, singly charged beam and plume ion density contours, and ion velocity vectors in a simplified case with conductor and insulator boundary conditions, respectively, at the inner pole and outer poles. Left: with space charge algorithm, right: without space charge algorithm.

diameter of the inner pole, forced the plume ions generated in that region to move axially. In the solution given by the space charge algorithm, the plume ions follow curved paths that end at the poles. The two phenomena described above contribute to increased erosion rates with respect to the results shown in [11]. As for the outer pole, the insulator boundary condition does not force as large of a change in the potential as the 0V condition applied in the inner pole. Nonetheless, the gradient in the electric field is reduced in the axial direction and enhanced radially. It can be observed that plume ions in this region also follow curved paths towards the pole close to its inner edge.

C. **Sputtering yield models**

Erosion in Hall2De accounts for contributions from three charge states, Xe^{+}, Xe^{++} and Xe^{+++}, for each ion population. The sputtering erosion rate (ε) due to ion bombardment by ions of charge state i_Z and population i_F is given by,

$$\varepsilon_{i_Z,i_F} = j_{i_Z,i_F} Y, \tag{13}$$

where the incident ion current density perpendicular to the channel wall, $j_{iz,iF}$, is dependent on the ion number density ($n_{iz,iF}$) and the ion velocity ($u_{iz,iF}$) at the wall. The sputtering yield, Y, is a function of the ion impact energy $K_{iz,iF}$, and incidence angle, β. Y is expressed throughout the paper in mm^3/C unless otherwise noted. The total erosion rate is the sum over all populations and all charge states:

$$\varepsilon = \frac{\sum_j \sum_{i_Z=1}^{N_z} \sum_{i_F=1}^{N_F} \varepsilon_{i_Z,i_F} \Delta t_j}{\sum_j \Delta t_j}. \tag{14}$$

Using this formula, erosion rates are averaged over multiple time steps and the effects of plasma oscillations captured in Hall2De are captured accurately. Because ions must traverse a sheath before striking the wall, the total impact energy is the sum of the kinetic energy ions have acquired in the plasma upon entrance to the sheath, and the sheath potential energy. Since the space charge algorithm already accounts for finite sheath effects, a distinction must be made between finite and infinitesimal sheath cases. For the latter, the potential energy, transformed to ion kinetic energy as the plasma ions are accelerated inside the sheath towards the solid material, is computed based on the Hobbs and Wesson solution to the 1-D sheath equations in the presence of secondary electron emission [22]. In the numerical simulations, the edge-centered ion velocity and the element-centered ion number density at each computational element adjacent to the wall boundary are used to determine the total impact energy, $K=K_{plasma}+K_{sheath}$, and angle, β. In the finite sheath case, the potential energy K_{sheath} is replaced by the difference between the wall potential and the cell-centered value of the space charge potential of the adjacent cell, $K_{sheath}=q_{iz,iF}(\phi_{SC,k}- \phi_{wall})$. The sputtering yield is determined as follows:

$$Y = f_\beta(\beta) f_{\mathrm{K}}(K), \tag{15}$$

where $f_\beta(\beta)$ and $f_{\mathrm{K}}(K)$ are fitting functions for the angle and energy dependence at zero angle of incidence, respectively. In the wear test, the magnetic poles were protected by a carbon cover. In addition, molybdenum plates were placed at different locations since the sputtering yield for xenon on this material has been experimentally determined for a wide range of ion energies. Experimental data for carbon and molybdenum by Doerner et al. [13] is shown in Fig. 5 accompanied by the continuous fits to the data used in Hall2De. The expressions used for the sputtering yield in Hall2De [11] are not physics-based and were motivated by the difficulties encountered at the time of fitting the experimental measurements making use of physics-based models, such as Bohdansky et al.'s [23]. No published data were found for the angular dependence of Xe on carbon and molybdenum so we have incorporated a fit of Garnier et al.'s data for sputtering of Xe on boron nitride [24] to Yamamura's function [25] for the angular yield. These fitting functions are as follows, with coefficients shown in Table I:

$$\begin{aligned} f_\beta(\beta) &= \cos(\beta)^{-c_0} \exp\left[-c_1\left(\cos(\beta)^{-c_2}-1\right)\right], && (a) \\ f_{\mathrm{K,iz}}(K) &= \frac{A}{iz}\exp\left[B + \frac{C}{\left(c_3 \ell n(K) - c_4\right)^{c_5}} + D\exp\left(c_6 K\right)\right]. && (b) \end{aligned} \tag{16}$$

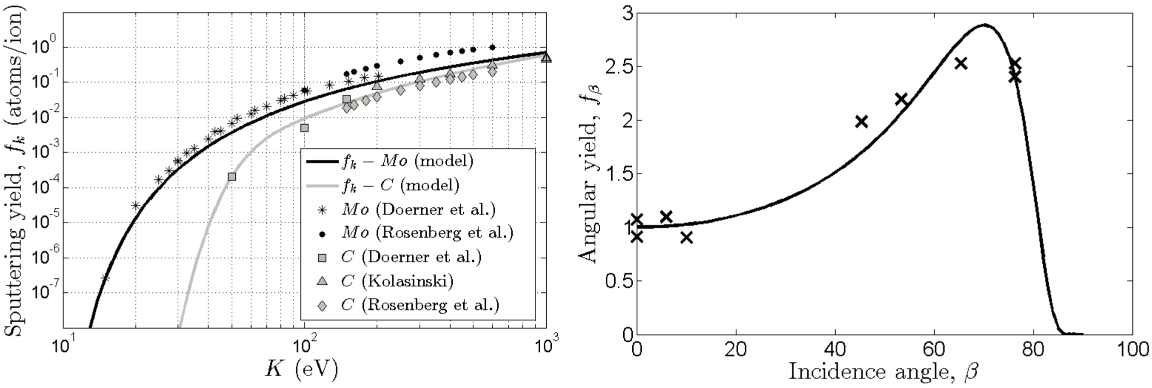

Fig. 5. Left: Sputtering yield for perpendicular Xe ion bombardment on molybdenum (Mo) and carbon (C). Comparison between implemented fit (Eq. (a) and Table I) and experimental data. Right: Angular yield model using Yamamura function [25] and comparison with experimental measurements by Garnier et al. [24].

Table I. Coefficients in the sputtering yield fitting function f_K(K) in Eq. (4b).

	A	B	C	D	c_0	c_1	c_2	c_3	c_4	c_5	c_6
Mo	0.097	8.101	-38.744	0	2.5204	0.8552	1	4.3429	9	0.5	0
C	0.055	7.788	-57.383	-147.94	2.5204	0.8552	1	1	0	1	-0.09

III. Steady state plasma solution at nominal operating conditions and predicted erosion rates

Previous numerical simulations of the H6 with a magnetically shielded configuration (H6MS) [11] showed that the erosion rates at the inner pole were comparable to those found in the unshielded configuration. Results for carbon and iron were reported, with erosion rates in the order of 10^{-13} mm/hr and 10^{-6} mm/hr, respectively. These values are orders of magnitude lower than the rates measured in the second 150-hour wear test (iron and molybdenum sputtering yield being comparable). This first set of simulations, which did not make use of the space charge algorithm described in Section II nor did it include the exact geometry of the thruster walls, argued that finite sheath effects and the details of the geometry should properly be accounted for. Three major improvements are included here with respect to previous work: the thruster geometry, and in particular the boundaries between the acceleration channel and the inner pole cover have been replicated according to the exact specifications of the thruster; the space charge algorithm has been set in place; and we have made use of the knowledge acquired in the validation of Hall2De for the H6US (described in companion paper [26]) to define the external boundaries of our computational domain and produce a plasma solution that is in closer agreement with experimental measurements. This plasma solution includes effects such as the anomalous resistivity generated in the cathode plume by the inception of ion-acoustic turbulence (IAT). All the simulations reported are run at the nominal 300V, 6kW conditions with a 75V threshold between beam and plume ion populations. A background pressure value of $1.5\text{x}10^{-5}$ Torr is assumed in all simulations and is close to the value measured in the vacuum facility during the 150-h wear test

A. **Computational domain**

The H6MS geometry is sketched in Fig. 6. The acceleration channel features a chamfered region at its exit typical of a “magnetically shielded” design. The inner pole carbon cover is 0.08*L*-thick and its exposed surface is

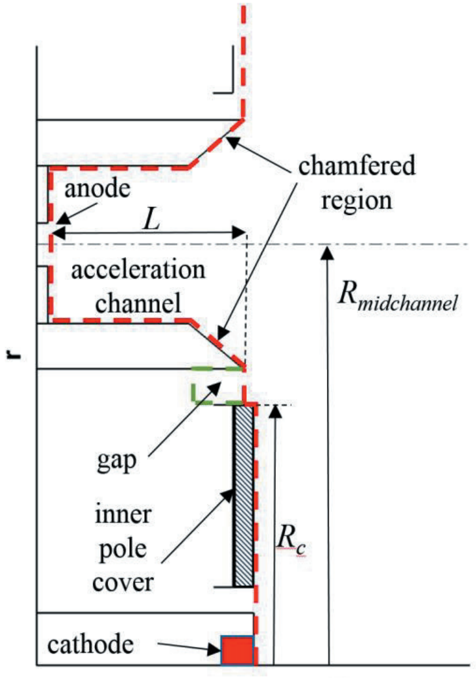

Fig. 6. Thruster geometry and computational domain with gap (dashed green contour) and without gap (dashed red contour)

located axially at a distance *d/L*=0.03 downstream of the channel exit. There exists a gap between the inner pole outer edge and the exit section of the acceleration channel. In our first series of simulations, this gap was not modeled; it was substituted by a flat surface at the axial location of the exit plane (dashed red contour in Fig. 6). This boundary has been modeled as either an insulator or a conductor in a first attempt to cover the range of potentials that could be established in this region in the presence of the gap. The results from this first series of simulations suggested that the details of the gap geometry could be important. Another series of simulations was conducted therefore this time incorporating the actual gap (dashed green contour in Fig. 6). Erosion rates for all three configurations are shown later in this section.

B. **Plasma solution**

Experimental evidence suggests that the discharge conditions measured in Hall thrusters are not possible when only classical collisions are considered in the determination of the electron transport coefficients. Additional mobility of electrons across magnetic field lines must be achieved through arguably collisionless mechanisms. The plasma solution produced by Hall2De implements the specification of an anomalous collision frequency profile that accounts for the aforementioned collisionless transport. Efforts at producing a first-principles model that could replicate the growth and transport of the instability mechanisms leading to the observed enhanced mobility of electrons are ongoing (see companion paper [27]) but have not yet been completed. Therefore our approach here is to use the profile that has been determined largely by comparison of simulation results with experimental measurements. In addition, knowledge gained from validation simulations of the H6US [26] can be extrapolated to the plasma solution in the magnetically shielded configuration. Specifically, it has been observed that the dimensions of the computational domain must comprise 7 to 10 times the length of acceleration channel in the radial and axial directions in order to avoid interference of the outflow boundary conditions with the plasma properties in the plume. This criterion typically indicates that the region of interaction between the ion beam and the plume of a cathode mounted at the thruster axis must be contained within the computational region. Failure to do so produces erroneous results as the electrons are forced to cross magnetic field lines in order to neutralize the beam. A second conclusion extracted from the validation simulations in the H6US is the insensitivity of the discharge to restricting the anomalous collision frequency to the regions in which the ion current is high (namely the main beam). This strengthens our previous hypothesis that the bulk of electrons that move from the cathode plume to the acceleration channel do so along the beam [28] and that ions play a role in the transport and generation of the collisionless transport. The third important result stems from the conclusions of our extensive experimental, numerical, and theoretical analysis of anomalous transport phenomena in the cathode plume, which suggests that the electron transport downstream of the keeper orifice in hollow cathodes cannot be explained by classical collisions only [29,30]. Ion-acoustic turbulence (IAT) as the source of the anomalous transport was measured in [31,32]. A simple model based on Sagdeev's expression for the saturation of the ion-acoustic instability [33] was implemented in Hall2De. The addition of anomalous resistivity mechanisms in the cathode plume allowed us to capture the plasma potential gradient at the boundary of the cathode plume and posterior ~30V plateau observed in experimentally measured radial profiles in the near plume of the H6US (Fig. 7 (right)). Similar measurements are not currently available for the magnetically shielded configuration, and for the purpose of this set of simulations, we have assumed that a similar plateau exists in the H6MS.

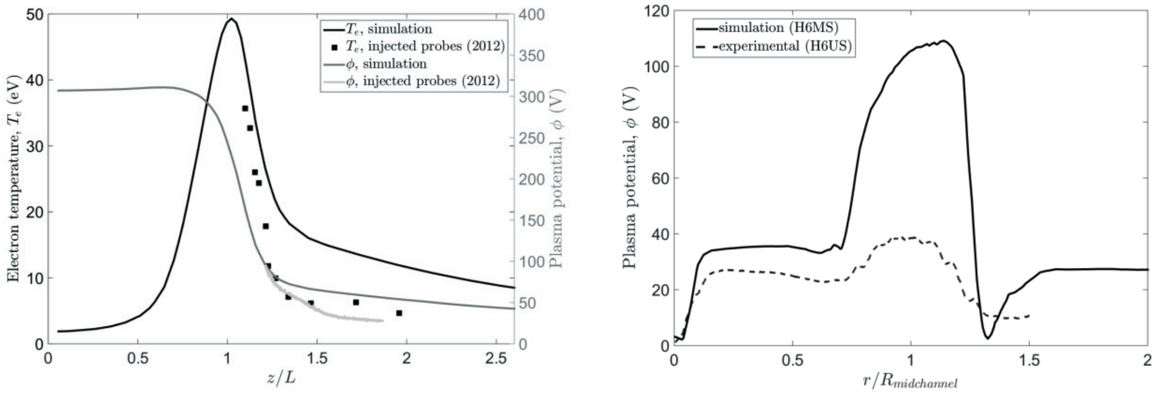

Fig. 7. Left: plasma potential and electron temperature along the channel centerline as predicted by Hall2De simulations and experimental measurements of injected probes [7]. Right: radial profile of the plasma potential at a plane 0.19L downstream of the channel exit. Simulation results are compared with the H6US measurements as experimental results for the H6MS are not currently available. The value of the plasma potential around the channel centerline is larger in the H6MS as the location of the acceleration region moves downstream in the magnetically shielded configuration due to the different magnetic field topology.

Figure 7 depicts a comparison between experimental measurements from injected probes and numerical simulations along the channel centerline. We have focused our efforts on achieving good agreement with the location of the temperature and potential gradients downstream of the acceleration channel as it is known at this state that injected probes perturb the plasma upstream of the location of the peak magnetic field [34]. We also show the radial profile of the plasma potential at a location z/L=1.19 from the anode. Currently, there are no measurements available of such profiles for the H6MS so we have included a comparison with the radial profile in the H6US to highlight that we reproduce in our simulations a plateau in the inner pole region similar to the one measured in the unshielded thruster. The effect on the erosion of modifying the value of this plateau will be explored in Section V. The potential around the channel centerline is larger in the H6MS since the peak value of the magnetic field is further downstream in the magnetically shielded configuration. As can be observed in Fig. 8, the performance variables (discharge current and thrust) exhibit an oscillatory behavior. It is discussed in [26] that these oscillations are cathode driven with a dominant mode at approximately 15 kHz and root mean square (RMS) amplitude at 8% of the nominal 20A value. These values are consistent with measurements reported in [35] for similar operating

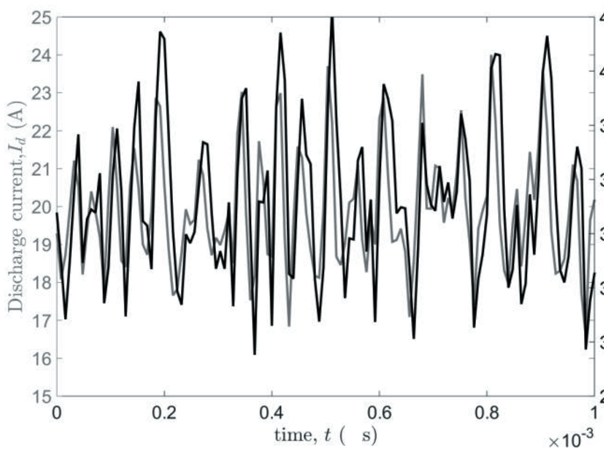

Fig. 8. Time-dependent behavior of discharge current and thrust in the H6MS at 300V, 6kW conditions. It can be observed that the discharge current leads the oscillations, which are followed with minimal lag by the thrust. The effect of these plasma oscillations on the erosion is captured by the use of Eq. (14)

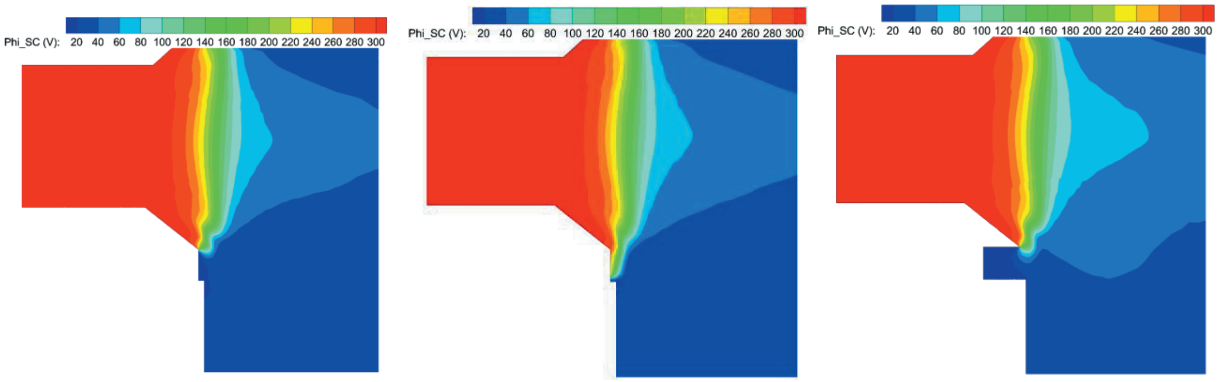

Fig. 9. Time-averaged plasma potential contours in Hall2De simulations with a space charge algorithm. Left and middle: flat vertical surface instead of gap with conductor and insulator boundary conditions, respectively. Right: computational domain with gap. The inner pole is always modeled as a conductor at 0V.

conditions. The effect of these oscillations on the erosion (as the energy of ions impacting the walls can change within a cycle) is captured in Eq. (14). These results are insensitive to the geometry of the inner pole walls as these only have a local effect on the plasma parameters.

C. **Sensitivity of the plasma solution to the geometry and boundary conditions**

In this paragraph, we discuss the differences observed in the solution of the plasma fields in the proximity of the inner pole when the geometry of the computational domain and the boundary conditions are modified. The translation of these plasma properties to erosion rates follows in subsection IIId and IIIe. This study has the aim of assessing the sensitivity of the plasma parameters and erosion rates to the accurate modeling of the thruster walls. In particular, two sensitivities are addressed. First, the surface of the carbon cover used in the wear test is located downstream of the exit plane. This geometrical feature can facilitate the bombardment of the surface by beam ions that are accelerated radially with respect to a geometry in which the pole surface is in the same plane as the channel exit or slightly upstream. The second is regarding the effect(s) of the specific boundary conditions implemented in the vicinity of the gap that separates the pole cover and the boron nitride piece used for the chamfered channel walls.

As seen in Fig. 9, the type of boundary assumed impacts significantly the topology of the plasma potential near the downstream chamfer corner. The plasma potential contours in the proximity of the inner pole and channel exit are shown here for the three cases examined. The plasma conditions at the channel centerline remain relatively unmodified but large topological changes locally occur in regions affected by the space charge algorithm. If the gap is modeled as a conducting wall (left), the result is similar to what was obtained in the simplified case depicted in Fig. 4, with the plasma potential exhibiting a "lobe" due to the 0V condition at the wall. If the wall is modeled as an

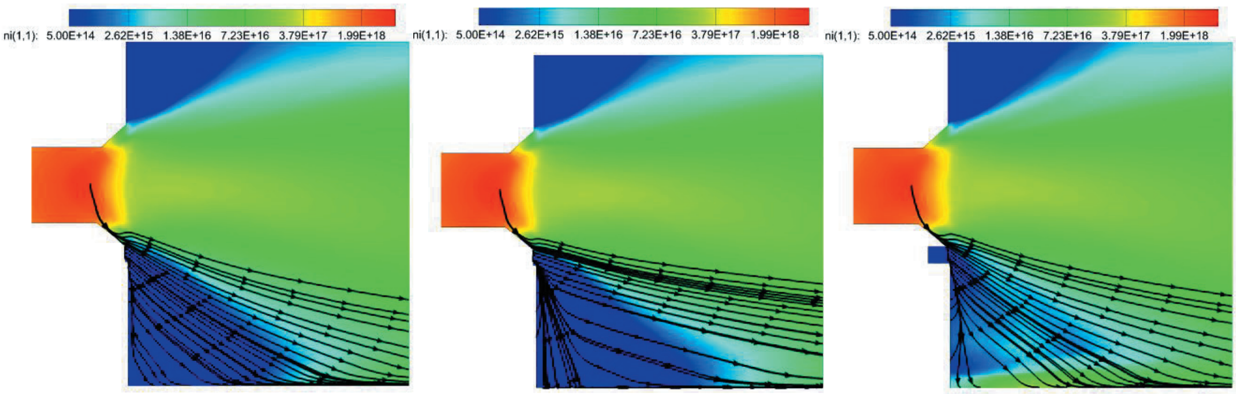

Fig. 10. Time-averaged number density (in m^{-3}) of singly charged beam ions and relevant ion trajectories. Left and middle: flat vertical surface instead of gap with conductor and insulator boundary conditions, respectively. Right: computational domain with gap. The inner pole is always modeled as a conductor at 0V.

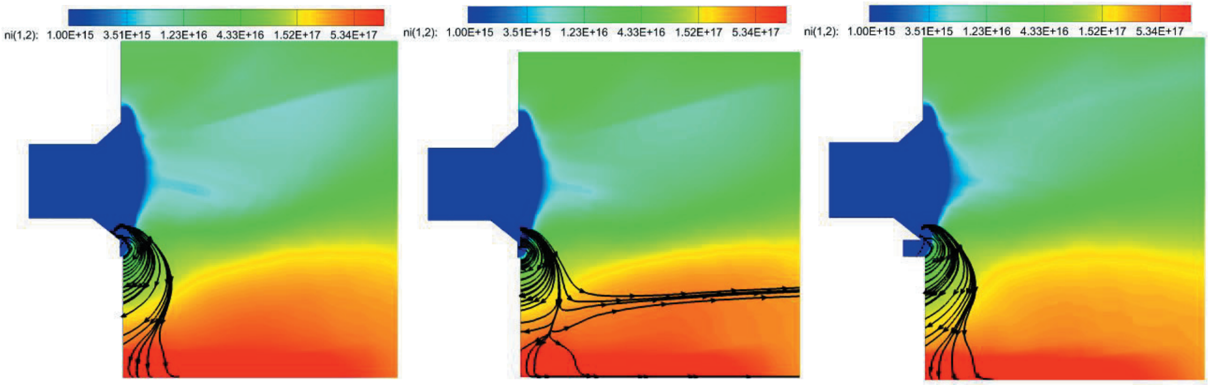

Fig. 11. Time-averaged number density (in m^{-3}) of singly charged plume ions and relevant ion trajectories. Left and middle: flat vertical surface instead of gap with conductor and insulator boundary conditions, respectively. Right: computational domain with gap. The inner pole is always modeled as a conductor at 0V.

insulator (middle case), the plasma contours extend to the inner pole surface. In this case, the radial gradients of the potential are lower, but ions generated close to the vertical surface that substitutes the gap can be accelerated directly towards the lateral surface of the carbon cover. The plasma potential when the gap is included in the computational domain resembles the conductor case, with a similar lobe that can potentially deflect beam ions towards the inner pole.

Figures 10 and 11 depict the distribution of singly charged beam ions and plume ions in the computational domain along with ion trajectories. The density and trajectories of doubly and triply charged ions are not shown as they are qualitatively similar. It can be observed that the differences in plasma potential shown in Fig. 9 arise in regions of low ion density. In consequence, the trajectories indicate that not many high-energy ions strike the pole walls. The bulk of the density in the pole region is therefore due to plume ions. As the time-averaged trajectories show, ions generated just downstream of the acceleration region are deflected by the electric fields towards the pole region. The increased density close to the cathode region also suggests that cathode ions, or the compressing effect of the decreasing radius, contributes to the erosion of the lower half of the pole cover.

D. **Ion current density and energy at the pole surface**

Before discussing the erosion rate predictions for the three configurations, we found illustrative to analyze the current density and average energy of each of the ion populations bombarding the pole surface. Here we present the results of this analysis in the computational domain with gap. Results for the other two cases are found to be

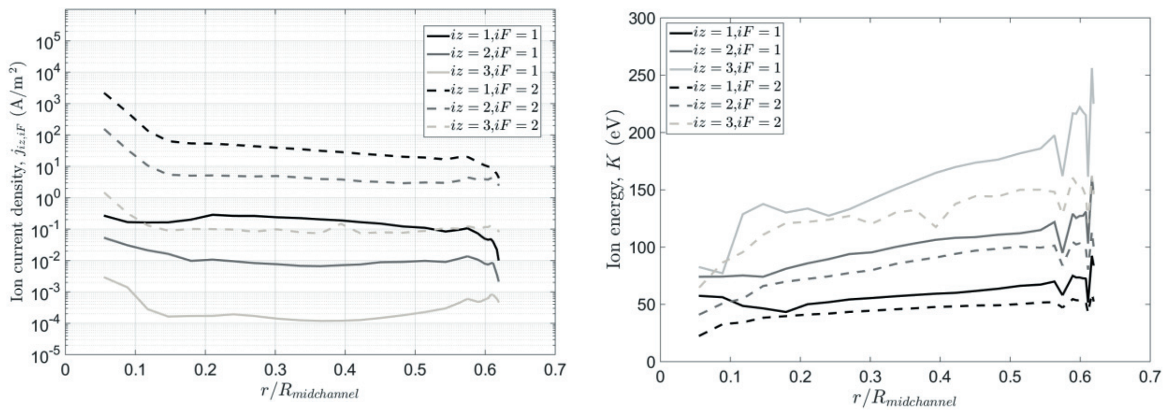

Fig. 12. Left, ion current density; right, ion energy, $K=K_{plasma}+K_{sheath}$, for each ion population (iz=charge number, iF=1,2 for beam an plume ions, respectively) in the computational domain with gap.

qualitatively similar.

The evolution of the ion current density is shown in Fig. 12 (left). As predicted by the visual examination of Figs. 10 and 11, the majority of the current to the walls is due to plume ions. Singly charged ions are dominant, with their current density being one order of magnitude larger than that of doubly charged ions. The current of beam ions is even lower, two orders of magnitude less in the case of singly charged beam ions. It is important to note that the total current to the walls is one order of magnitude larger than the one inferred from combining the averaged erosion rates during the wear test for molybdenum and carbon, which was approximately 7A/m^2. The ion energy (Fig. 12 (right)) is however much lower than the experimentally predicted value of ~120eV. The energy of the singly charged plume ions has an average value of approximately 40V, with the energy of doubly and triply charged ions being higher by a factor of approximately 2 and 3, respectively, since the latter gain more kinetic energy for the same variation of the plasma potential. As for beam ions, their energy is also low and may appear surprising that the average energy of singly charged ions is lower than the threshold set in place between the two ion populations (75V). This phenomenon can be explained by the plasma oscillations in the inner pole region and the manner the threshold between populations is specified. It has been observed that during plasma oscillations, the plasma potential can exceed the threshold of 75V near the poles. In these events, ions of the high energy population are generated in the plume (i.e., these high energy ions are not, strictly speaking, beam ions but are included in the high energy population). As the value of the potential decreases during the decaying part of the oscillation, the effective potential energy of those high energy ions decreases and their final velocity at the wall is not as large as if they had been accelerated by a 75V potential gradient. Only extremely close to the outer diameter of the pole does the energy of high energy ions increase substantially, indicating that some beam ions can impact this region.

Figure 13 shows the total erosion rates, and the contribution of each population to the erosion, for sputtering on molybdenum and carbon. Due to the higher current densities, erosion rates are driven mostly by plume ions. It can be observed however that the contribution of doubly charged ions to the erosion is not negligible despite their current density being typically one order of magnitude less than that of singly charged ions. This is attributed to the steep increase that the sputtering yield exhibits at ion energies of 40 to 60 eV (Fig. 5), where a change of 10eV produces increments of approximately one order magnitude. The contribution of the beam ions to the erosion is insignificant.

With respect to the measurements, the erosion rate is under-predicted by factors of 3 to 5. The comparison is slightly worse for carbon. Indeed, the lower average energy with respect to the experimental prediction of ~120V, which would result in under-predicting the measurements by more than an order of magnitude at equal current density conditions, is somewhat compensated by the higher current to the walls predicted in the simulations. The average ratio between the computed erosion in molybdenum and carbon is approximately 7, which would correspond to an average energy of 70eV, according to the relation between ion energy and the ratio of sputtering yields in Fig. 2. This appears in principle not consistent with the 40eV average energy shown in Fig. 12 (right) for singly charged ions. Two reasons have been identified that explain this discrepancy. In the first place, the contribution of doubly charged ions is not negligible and their average energy is higher than 40eV. Secondly, the

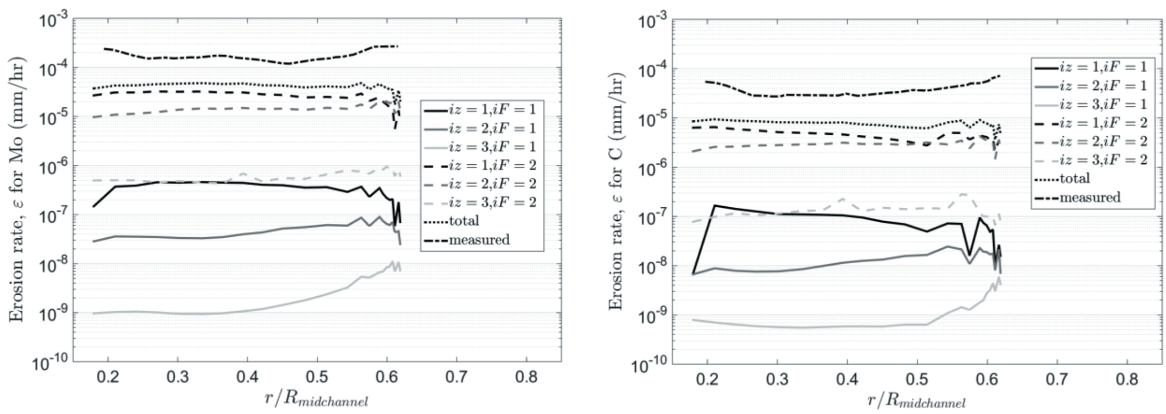

Fig. 13. Erosion rates for each ion population (iz=charge number, iF=1,2 for beam and plume ions, respectively) in the computational domain with gap. Left: rates on molybdenum, right: rates on carbon

plotted values of the energy are time-averaged. The periodic oscillations cause ions with energy higher than 40eV to strike the walls from time to time. This effect is successfully captured by Eq. (14). In fact, if the erosion is computed instead as,

$$\varepsilon = \sum_{i_Z=1}^{N_z}\sum_{i_F=1}^{N_F}\varepsilon_{i_Z,i_F} = \sum_{i_Z=1}^{N_z}\sum_{i_F=1}^{N_F}\bar{j}_{iz,iF}\,Y\left(\overline{K}_{iz,iF},\overline{\beta}_{iz,iF}\right), \tag{17}$$

with $\bar{j}_{iz,iF}$, $\overline{K}_{iz,iF}$ the values depicted in Fig. 12, the ratio between the erosion rate of molybdenum and carbon increases to approximately 10 and the differences with respect to the measured values increase, under-predicting results by factors of 5 to 10. This result stresses the importance of capturing the time-resolved oscillations in the erosion measurements rather than computing erosion rates using time-averaged quantities.

The erosion rates reported here represent a large improvement, in terms of level of agreement with the experimental measurements, with respect to those in Fig. 13 of [11]. For carbon material (molybdenum was not considered in [11]), negligible erosion was predicted for the most part of the pole cover. Only close to the outer diameter the erosion was significant. However, the latter effect was due to the high ion energy (close to 300V), which was determined as the difference between the wall potential (0V) and the plasma potential in the adjacent cell. This value of the potential was large (similar to that reported in Fig. 4 (right)) as neither the gap (and related boundary conditions) nor the space charge algorithm had been implemented at the time. These improvements in our capability to produce results more according to the experimental evidence stresses the importance of capturing the local sheath effects.

In the process of validating our erosion rates results, we performed several tests not reported here, such as modifying the threshold energy between ion populations or using a particle-in-cell (PIC) approach instead of the hydrodynamic formulation for the low energy ions. Results were fairly insensitive to these changes.

E. **Comparison of erosion rates for different geometries and boundary conditions**

The erosion rates for the three cases examined - no gap in the geometry with conductor and insulator conditions in the flat surface that replaces the gap, and computational domain with gap - are presented in Fig. 14. Only total erosion rates are shown (with no mention of the contribution of each of the populations) as the results of the previous paragraph underscore that erosion is mostly driven by (low-energy) plume ions. The comparison between the three cases reveals that higher erosion rates are obtained in the gap configuration. However, results for the other configurations remain within a factor of 5, which is still within our uncertainties especially in light of the extreme sensitivity of the sputtering yield in the ion energy range of 40 to 60eV and the lack of measurements of the sputtering yield at low energies (note that for carbon, no data below 50eV is available).

We can make use of these results to establish a lower and upper bound on the agreement of our simulations with respect to the measurements. In doing that, we determine that we are under-estimating the erosion rate by factors of

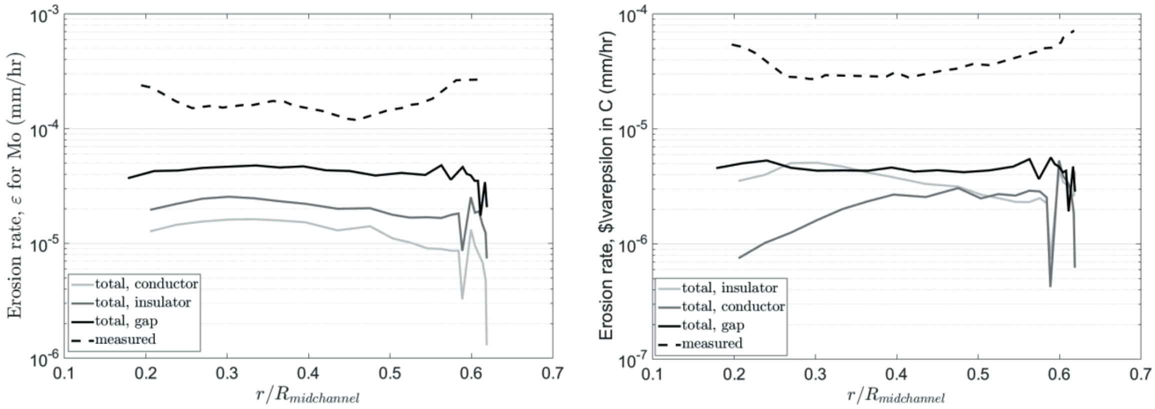

Fig. 14. Erosion rate comparison along the inner pole for the three configurations examined: conductor/insulator= domain with no gap and conductor/insulator boundary conditions instead; gap: computational domain with gap. Left: rates on molybdenum, right: rates on carbon

3 to 15. In the next sections, we explore mechanisms that can potentially enhance the erosion rate. Two mechanisms that may lead to higher erosion rates than what we compute are being considered: the presence of more beam ions in the inner pole region and the existence of high-frequency oscillations (not captured by the hydrodynamic formulation of Hall2De) that may produce high-energy plume ions. These two hypotheses will be explored in Section IV and V, respectively.

IV. Investigations of erosion-enhancing mechanisms due to beam ions

There exist two possible mechanisms that can lead to an increased presence of beam ions in the inner pole region: an increased divergence of the ion beam and the presence of oscillations that change the location of the acceleration region in time. In the following paragraphs, we explore each of these effects and investigate whether the plasma conditions that lead to increased erosion rates are consistent with experimental evidence, such as plasma and performance measurements.

A. Increased beam divergence

Numerical simulations like those performed with Hall2De and similar Hall thruster codes, are challenged by our inability to self-consistently compute the anomalous electron transport coefficients. As a result, our simulations rely on experimental measurements to guide the variation of the anomalous collision frequency in the computational domain [6,20] which, in turn, affects the location of the discharge relative to the anode. Recent experimental evidence has shown that probes injected into the discharge of the H6 can perturb the plasma [34]. Therefore, in both the experiments and the numerical simulations there remains an uncertainty on the precise location of the acceleration region. In this section, we investigate the sensitivity of the pole erosion on the location of the plasma. As it is known that moving the location of the acceleration region downstream leads, among other effects, to higher beam divergence, we attempt to capture a location of the acceleration region downstream of the nominal location used in the previous section (Fig. 7) for which we start observing a non-negligible amount of beam ions in the pole region. This numerical test is performed by translating the distribution of the anomalous collision frequency accordingly along the channel centerline. If it is shown that the required translation of the acceleration region to enable a significant presence of high energy ions in the pole region is within the uncertainties associated with the injected probe measurements (which can exceed a few millimeters), we can argue that the higher erosion rates observed in the wear test can be attributed to bombardment of high-energy beam ions.

In a series of numerical experiments, the anomalous collision frequency profile was moved downstream along the channel centerline. Reported here are the results with shifts of $0.25L$ and $0.5L$ (additional intermediate cases were run in order to confirm the observed trends) and their comparison with the nominal case described in the previous section. The computational domain with gap between the chamfered acceleration channel and the inner pole was used in all the simulations.

The evolution of the plasma potential contours as the anomalous collision frequency profile is moved downstream is depicted in Fig. 15. It is worth mentioning that the shifting occurs along the channel centerline but the formulation used to assign values of the anomalous collision frequency to cells away from the channel centerline consists of propagating the channel centerline values following magnetic field lines [6]. Due to the convergence of the B-lines as they approach the poles, a shift at the centerline does not correspond to the same shift (in terms of axial distance) close to the walls. This feature produces lines of constant plasma potential that are more convex as the profile is moved downstream, increasing the divergence of the beam, as seen in Fig. 16. In consequence, more ions are being accelerated radially and the density of high energy ions increases in the region close to the poles. In contrast, the presence of plume or low-energy ions decreases (Fig. 17). As the plasma is moved downstream, the 75V threshold is also displaced, reducing the extent of the computational domain in which plume ions are generated. In fact, the analysis of the averaged trajectories indicates that ions generated in the proximity of the cathode in the downstream configurations (middle and right columns) are the main contribution to the low-energy ions bombarding the pole cover. The contribution of ions generated just downstream of the threshold contour decreases as the profile is moved downstream. This results in the average energy of the ions impacting the walls being reduced, as the potential in the cathode region is low and therefore ions do not gain significant velocity before impacting the wall.

Figure 18 shows the erosion rates for the three examined cases. Contributions of the high and low energy ion populations (adding the results of each of the charge states) to the erosion are also plotted. These results indicate

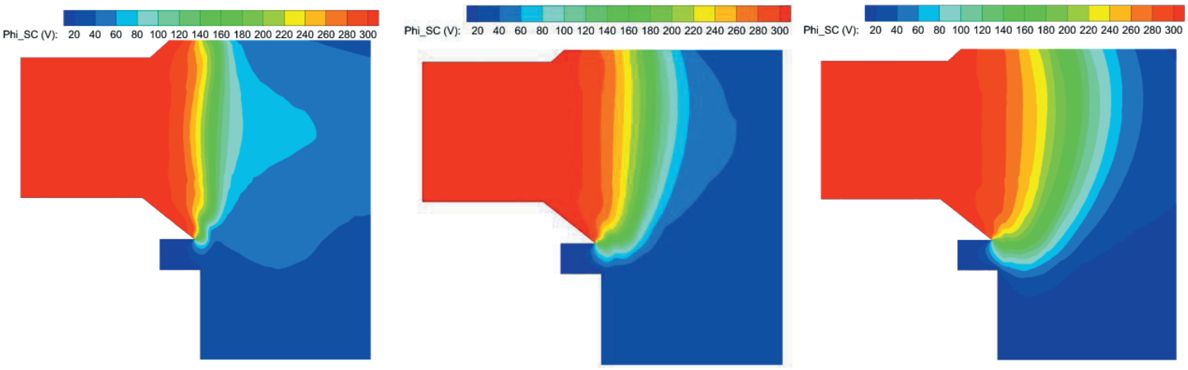

Fig. 15. Time-averaged plasma potential contours for: left, nominal anomalous collision frequency profile; middle, profile moved downstream by 0.25L; and right, profile moved downstream by 0.5L

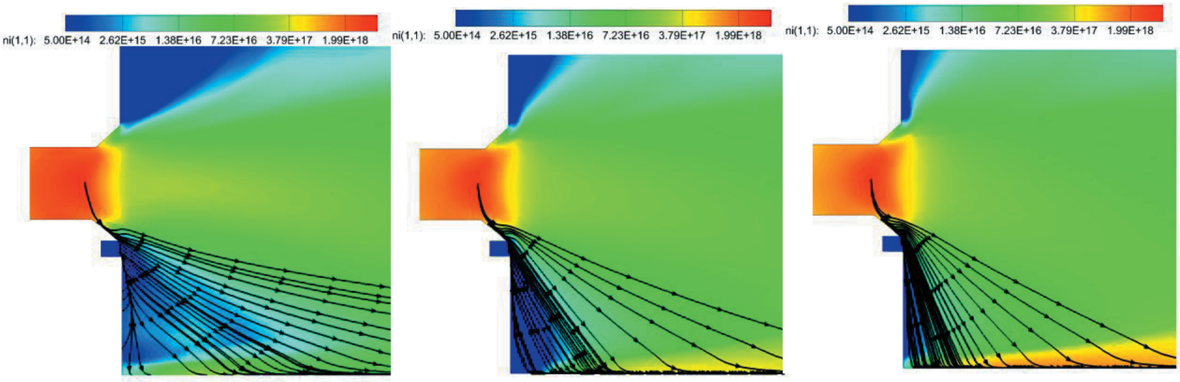

Fig. 16. Time-averaged contours of density of singly charged beam ions (in m^{-3}) for: left, nominal anomalous collision frequency profile; middle, profile moved downstream by 0.25L; and right, profile moved downstream by 0.5L

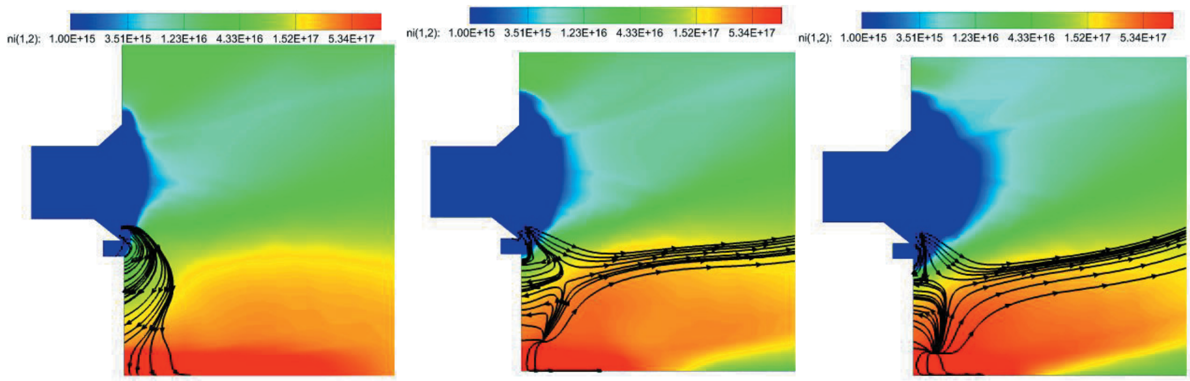

Fig. 17. Time-averaged contours of density of singly charged plume ions (in m^{-3}) for: left, nominal anomalous collision frequency profile; middle: profile moved downstream by 0.25L; and right: profile moved downstream by 0.5L

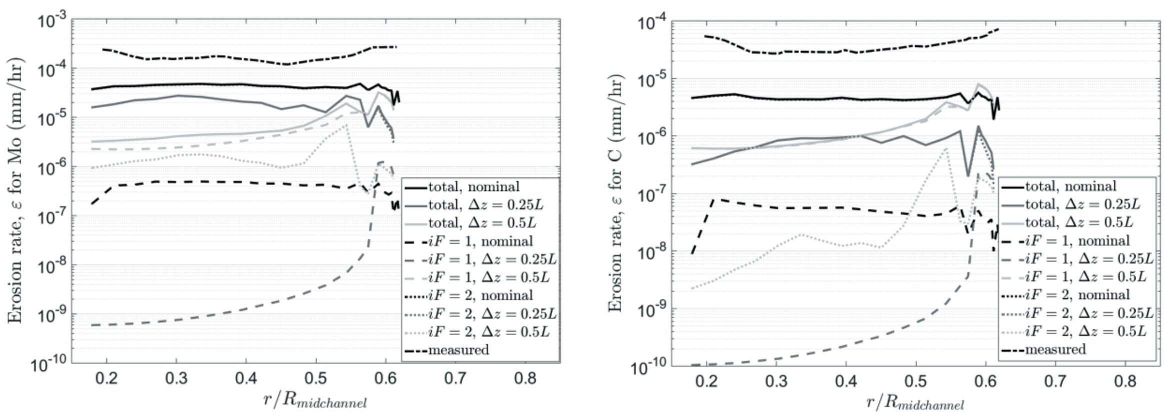

Fig. 18. Erosion rate comparison along the inner pole for three plasma profiles in the computational domain with gap. As the plasma is moved downstream, the contribution of beam ions increases and that of plume ions decreased. Left: rates on molybdenum, right: rates on carbon

In the nominal case and the case with a shift, Δz, equal to 0.25 times the length of the channel, the contribution of beam ions (iF=1) is negligible. Only when the profile has been moved by half the channel length, the contribution of beam ions to the erosion becomes dominant. However, as this occurs, the contribution of plume ions (iF=2) decreases due to the reasons exposed in the previous paragraph. The increased erosion due to beam ions only compensate entirely for the loss of plume ions close to the outer diameter ($r/R_{midchannel}$>0.55).

The conclusion of this investigation is that in order to drive beam ions to the pole region, the potential gradient that accelerates the beam must have been displaced downstream from its nominal position (Fig. 7) by more than the spatial uncertainties allowed in plasma measurements by injected probes. In that case, the increased erosion rate due to beam ions does not compensate for the loss of plume ions (which have lower energies but produce more current to the walls). Taking everything into account, uncertainties in the location of the plasma are an unlikely reason for explaining the differences between the erosion rates predicted by the simulations and the actual measurements.

B. **Plasma oscillations that can change cyclically the location of the acceleration region**

Low-frequency plasma oscillations are already captured in Hall2De simulations (Fig. 8). However, these oscillations do not alter the physical location of the acceleration region as this feature is controlled by the anomalous collision frequency profile, which remains fixed. In this section, we report the results of a numerical investigation that consists of shifting the anomalous collision frequency profile upstream and downstream of its nominal location with a sinusoidal signal in time of frequency similar to the observed oscillations (~15kHz). By introducing this feature in our simulations, we attempt to reproduce a situation in which the average location of the plasma does not change with respect to the nominal case (Fig. 7) while oscillations may enhance the erosion rates.

Similarly to the previous subsection, several numerical tests were run with incremental oscillation amplitudes. The results reported here are for $\Delta z=0.25L$. We have chosen this case as it illustrates that abnormally large oscillations would be required to obtain good agreement with experimental measurements. In fact, Fig. 19 (left) depicts the time signal of the discharge current and thrust. The discharge current oscillations have amplitudes that exceed 100A peak-to-peak and equally large oscillations are found for the thrust. The average value of the discharge current is slightly above 20A, which indicates that the objective of obtaining a time-average plasma solution equal to Fig. 7 is not completely attained. These oscillations are not consistent with those observed in tests of the H6MS performance at similar operating conditions [35], which indicate that the RMS amplitude of the oscillations is approximately 1.6A. Figure 19 (right) shows the total erosion rates and the contributions of each population for molybdenum (black) and carbon (grey). In this case, the predicted rates are comparable to those measured on molybdenum and off by a factor of 2-3 on carbon. It can be observed that under the forced oscillations, the contributions of beam and plume ions become comparable. These results can be regarded as a combination of the nominal and $\Delta z=0.5L$ cases in subsection IV,a. In the course of one oscillation, when the plasma is moved downstream, beam ions dominate the erosion and when the profile moves back upstream, the erosion is controlled

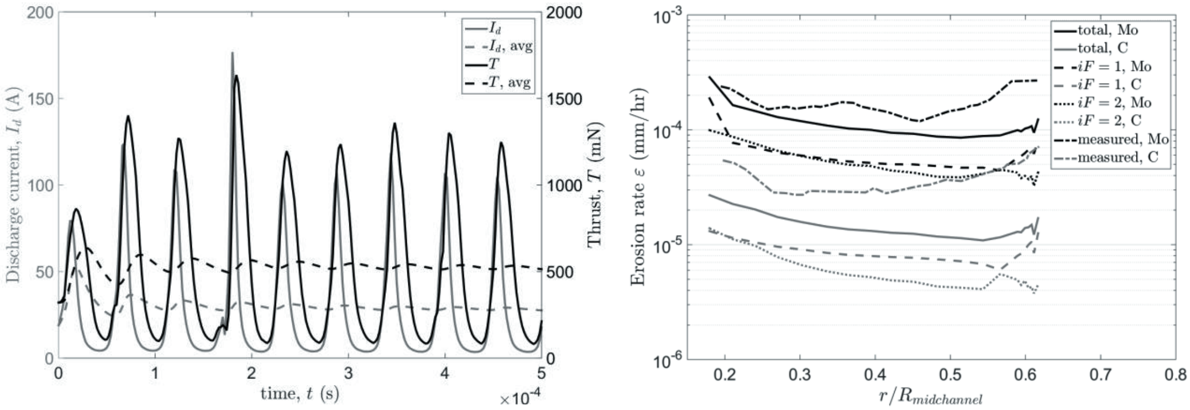

Fig. 19. Left: induced oscillations in discharge current and thrust. The amplitude of such oscillations is not consistent with experimental measurements. Right: Erosion rates with induced oscillations in the plasma. Total values, as well as the contributions of the beam and plume ions, are shown.

by bombardment of plume ions. It can be observed though that the dynamic effect of the oscillations is conductive to more erosion at the inner pole than when the plasma is only statically shifted in location.

The conclusion of this analysis is that it is highly unlikely that dynamic shifts in the location of the plasma over the course of low-frequency oscillations can explain the discrepancies between predicted and measured erosion rates at the poles. The plasma oscillations required to obtain erosion rates comparable to the experiments are very large when compared to the mild oscillations reported in performance measurements of the H6MS operating at the 20A, 6kW condition. However, the results of this analysis indicate that erosion rates in the poles can be exacerbated in thrusters exhibiting large discharge oscillations during operation.

The two numerical experiments presented in this section indicate that bombardment of beam ions is not a likely cause for the significant roughening observed at the pole walls during the 150-hr wear test. Ruling out this hypothesis leads us to believe that plume ions are the major contributors to the erosion. This possibility will be explored in the next section.

V. Increased erosion rates due to plume ions

It was shown in Section III that plume (low-energy) ions were the major source of erosion on the inner pole, as predicted by H6MS simulations. This result holds for the nominal location of the acceleration region (Fig. 7) irrespectively of the modeled geometry. Predicted erosion rates however under-estimated the measured values by factors of 3 to 15. In this section, we examine the plasma conditions that would be required to overcome the discrepancies observed with respect to the experimental results.

In the first subsection, we investigate one of the major uncertainties in our simulations: the value of the plateau in the plasma potential (Fig. 7(right)) in the vicinity of the inner pole. In Section III, this value was assumed to be similar to the plateau observed in the H6US (~30V). In consequence, we analyze whether a theoretical increase in this plasma property would produce the desired erosion rates. In the second subsection, the possible effect of cathode-driven, ion-acoustic turbulence (IAT) oscillations of high frequency is examined with an idealized model.

A. Value of the plateau of the plasma potential in the vicinity of the inner pole

It is shown in Fig. 20 that the value of the sheath potential, K_{sheath}, is the principal contribution to the kinetic energy of ions, K, impacting the walls for the most part of the pole surface. This quantity is computed as the difference between the value of the plasma potential in the cell adjacent to the boundary edge and the imposed potential at the walls (0V), assuming a sheath of negligible width compared to the typical cell size. Close to the outer diameter, the value of K_{sheath} decreases as the sheath becomes finite. In this region, K_{sheath} no longer represents the energy gained due to ion acceleration in the sheath since the latter becomes finite. The plasma potential is

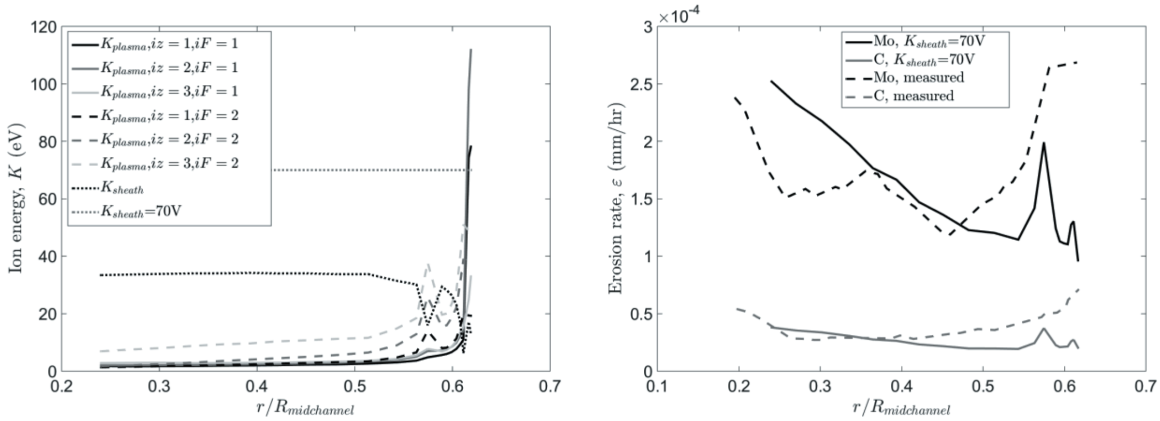

Fig. 20. Left: kinetic energy of each ion population compared to sheath potential. Theoretical sheath potential that would result in values of the erosion close to measurements also depicted. Right: Erosion rates on carbon and molybdenum when theoretical sheath potential of 70V is used and comparison with measured

computed by the space charge algorithm and, in consequence, most of the acceleration due to the finite sheath is contained in K_{plasma} instead.

We performed a simple experiment consisting of rising the value of K_{sheath} progressively until an acceptable agreement with the measured experimental values is attained. In order to produce such a result, the value of the plasma potential in the inner pole region shown in Fig. 7 would be required to increase accordingly. This test was performed without conducting additional simulations and thus assumes that variables such as the ion current density to the walls remain fixed when the plasma potential in the vicinity of the pole is raised. Erosion rates with K_{sheath}=70eV agree reasonably well with the measured values (Fig. 20 (right)). When the sheath potential is increased to such values, the contribution to the erosion of doubly charged ions becomes more important (as their effective energy is 2 K_{sheath}) than in the nominal case shown in Section III. Under these conditions, there exists a population of singly charged plume ions with ion currents in the order of 10-100 A/m^2 and energy ~70eV and another of doubly charged ions with current density in the order of ~5A/m^2 and energy ~140V. The contribution of triply charged ions is still negligible. The addition of the effects of the two dominant populations (converting the doubly charged ions into "effective" singly charged ions by reducing their current by one half) results in conditions of average ion current density and energy similar to those inferred from the experimental measurements (7A/m^2, 120V).

The reported 70V value of the plasma potential at the inner pole plateau is considerably large because it would result in low thruster efficiency as large potential values in the plume correlate negatively with beam ion velocities. However, the results shown here when combined with plasma measurements in the pole region (scheduled to be performed in the next months) can be readily used to confirm or rule out the presence of a large sheath potential in the inner pole as a possible cause for erosion

B. Ion-acoustic turbulence oscillations

Theory and numerical simulations performed in the past predicted the presence of anomalous transport mechanisms in the near-plume of discharge hollow cathodes [29,36-38]. Additional evidence of this phenomenon is found in numerical simulations performed with our companion code OrCa2D [30] in the fact that additional electron resistivity, which cannot be explained by classical collisions, is required to explain the discharge conditions found in cathode tests. The measured values of keeper erosion in some cathodes can neither be explained uniquely by the steady state plasma solution [37,38]. Recently, the source of the anomalous transport was experimentally identified as ion acoustic turbulence (IAT) [31,32].

The H6MS is a Hall thruster with the cathode mounted at the thruster centerline. In this geometrical configuration, the inner pole can be regarded as an extension of the cathode keeper and the same oscillations that produce the erosion of the cathode elements can be extended radially towards the pole.

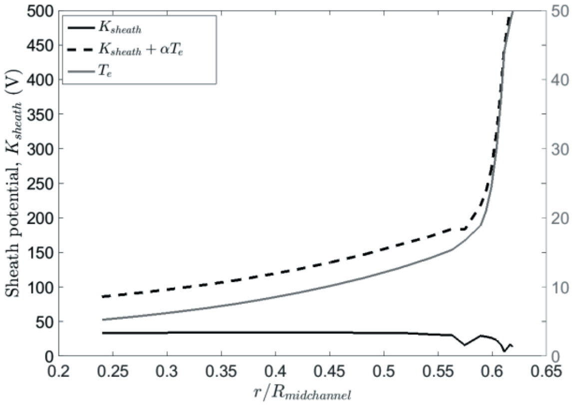

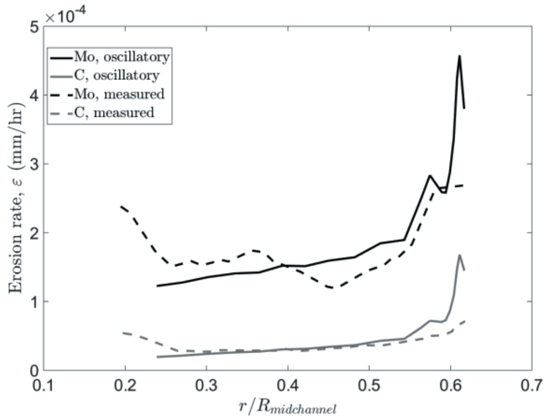

Fig. 21. Left: comparison between average sheath potential from Hall2De simulations and peak value during oscillations. Right: Erosion rates on carbon and molybdenum with sheath potential oscillations. Parameter α=10

In order to assess the possibility of cathode-induced oscillations playing a role in the erosion of the inner pole, we use the simple model proposed in [38]. This model postulates that plasma oscillations are of sinusoidal form and proportional to the electron temperature in a way such that

$$\hat{K}_{sheath} = K_{sheath} + \alpha T_e \sin\left(\frac{2\pi t}{\tau}\right), \tag{18}$$

with K_{sheath} being the time-averaged sheath potential from our Hall2De simulations, which can be found in Fig. 20 (left). The erosion rate for each ion population is then computed using the expression:

$$\varepsilon_{iz,iF} = \frac{1}{T}\bar{j}_{iz,iF} f_\beta\left(\bar{\beta}\right)\int_0^T f_k\left(\overline{K}_{plasma} + \hat{K}_{sheath}\right)dt, \tag{19}$$

where the values of the current and the kinetic energy of the plasma are time-averaged. It is important to note that the computed erosion rate is independent of the chosen period of the oscillations, T, and that the use of this formula for the erosion rate actually makes us lose the enhancement in the erosion due to low-frequency oscillations already captured in Hall2De (i.e., if the parameter α is set to 0, this expression is equivalent to Eq. (17) and not to Eq. (14)).

Figure 21 shows that reasonable agreement with experimental measurements is obtained with a value of the coefficient α in the order of 10, which translates in large plasma oscillations that can reach peak values of 100 to 150V. As the electron temperature increases close to the outer diameter, the oscillations grow larger and so do the predicted erosion rates. However, the likelihood of this model being valid that far from the source of oscillations (i.e., the cathode) is extremely small. The presence of plasma oscillations in the order of 100V is also difficult to justify, since they have not been reported in any cathode test to date.

The results of the numerical tests presented in the last two subsections indicate that large static (~70V) or oscillatory (~100V) values of the plasma potential in the vicinity of the inner pole are required to reproduce conditions that can lead to the measured erosion rates. The reported necessary conditions are *a priori* unlikely, based on past evidence, to exist in reality.

VI. Conclusions

In response to recent observations of inner pole sputtering during a 150-hour wear test of a magnetically shielded thruster (H6MS) operating at nominal conditions (300V, 6kW), we have performed numerical simulations in an attempt to understand the possible causes. The 2-D axisymmetric code Hall2De has been enhanced for this purpose with a new algorithm that accounts for finite sheath effects in the vicinity of the chamfered edges of the channel where the Debye length can become large compared to the characteristic size of the surrounding computational cells. This algorithm is based on the solution of Poisson's equation for the plasma potential in selected cells of the computational domain, which modifies the local topology of the plasma potential contours near the walls compared to the hydrodynamic solution. However, the new algorithm does not disturb global performance variables or the plasma solution far from the walls.

The H6MS geometry includes a gap between the inner pole and the acceleration channel. This gap was originally not included in the model and was replaced with a planar surface located at the channel exit plane. These simulations showed that the results were sensitive to our choice of boundary conditions so the gap was finally included in the computational domain. A first set of numerical simulations involving the computational domain with and without the gap (with insulator and conductor boundary conditions) were performed and the results showed that though changes in the plasma potential in the proximity of the gap did occur as expected, they were not large enough to alter the erosion rates significantly. It was shown that most of the erosion was produced by low energy ions generated in the plume regions and that beam ions carrying high kinetic energy seldom impact the pole walls. The comparison with the measured experimental values revealed that numerical results under-predicted the erosion rates by factors of 3 to 15, with results being in closer agreement when a molybdenum target is assumed instead of a carbon surface. A factor contributing to the uncertainty of our predictions is the lack of experimental data for the sputtering yield of xenon on carbon in the 50eV range.

Mechanisms that could possibly lead to increased erosion rates were investigated following the results of the first numerical experiments. Starting with the possibility of beam ions impacting the pole surfaces, we moved the acceleration region downstream of its nominal location (as determined by injected probes) in order to seek higher divergence angles in the beam. It was shown that beam ions would only start bombarding the pole surfaces if the acceleration region was located at a distance of approximately $0.5L$ (with L the length of the acceleration channel) downstream from its nominal position. Having an acceleration region so far downstream is inconsistent with plasma measurements along the channel centerline. We also artificially induced oscillations in the location of the acceleration region. When the plasma location describes oscillations with maximum amplitude of one-fourth of the channel length, the predicted erosion rates become comparable to their experimental counterparts. This suggests that dynamic effects may have more influence in producing increased erosion rates than just shifting the location of the plasma statically. However, it was also shown that the discharge current oscillations were in the order of 100A for a 20A discharge and not in agreement with performance measurements, which showed mild oscillations of approximately 1.6A RMS at the 20A, 6kW operating condition.

Finally, the possibility of increased rates of erosion due to the plasma conditions in the proximity of the inner pole was explored. One of the uncertainties in our Hall2De plasma simulations is the value of the plasma potential in this region, which was assumed in the first set of simulations similar to that experimentally observed for the unshielded version of the same thruster (~30V). It was found that the value of the sheath potential (assuming the pole surface grounded at 0V) should have an average value of 70V to reproduce the experimental measurements. The presence of high-frequency plasma oscillations and their contribution to increased erosion rates was also examined, determining that oscillations with amplitudes in the order of 100V must be present. These values are a priori abnormally high, but no measurement of the plasma potential in the vicinity of the pole has been performed to date in order to validate or discard this hypothesis.

The results reported here have been used to guide a series of plasma measurements that will be performed in the next months. This experimental campaign will consist of time-resolved plasma potential measurements in the poles, retarding potential analyzer (RPA) measurements, and the use of laser-induced fluorescence (LIF). The combination of these experimental techniques will shed light on the presence of high- and low-frequency oscillations and their amplitude, the ion energy distribution, the presence of beam ions in the vicinity of the poles, and the exact location of the acceleration region.

Acknowledgments

The research described in this paper was carried out by the Jet Propulsion Laboratory, California Institute of Technology, under a contract with the National Aeronautics and Space Administration. The support of NASA's Space Technology Mission Directorate through the Solar Electric Propulsion Technology Demonstration Mission (SEP TDM) project is gratefully acknowledged. The authors wish to acknowledge Dr. Michael Sekerak for the experimentally measured erosion rates featured in this paper.

References

[1] J. R. Brophy, and L. Friedman, "Returning an Entire Near-Earth Asteroid in Support of Human Exploration Beyond Low-Earth Orbit," in IAF Global Exploration Conference, Washington, D. C., 2012.

[2] J. R. Brophy, L. Friedman, and F. Culick, "Asteroid Retrieval Feasibility," in Aerospace Conference, 2012, Big Sky, MT, 2012, pp. 1 - 16.

[3] J. R. Brophy, and S. Oleson, "Spacecraft conceptual design for returning entire near-Earth asteroids", AIAA Paper No. 2012-4067, in Proceedings of the 48th AIAA Joint Propulsion Conference, Atlanta, GA, 2012, pp. 4067.

[4] I. G. Mikellides, I. Katz, R. R. Hofer, D. M. Goebel, K. H. de Grys and A. Mathers, "Magnetic shielding of the channel walls in a Hall plasma accelerator," *Physics of Plasmas,* vol. 18, no. 3, pp. 033501, Mar, 2011.

[5] I. G. Mikellides and I. Katz, "Numerical simulations of Hall-effect plasma accelerators on a magnetic-field-aligned mesh", Physical Review E, Vol. 86, 2012, p. 046703.

[6] I. G. Mikellides, I. Katz, and R. R. Hofer, "Design of a laboratory Hall thruster with magnetically shielded channel walls, phase I: numerical simulations", AIAA paper 2011-5809, in proceedings of the 47th AIAA Joint Propulsion Conference, San Diego, California, 2011.

[7] R. R. Hofer, D. M. Goebel, I. G. Mikellides, and I. Katz, "Design of a laboratory Hall thruster with magnetically shielded channel walls, phase II: experiments", AIAA paper 2012-3788, in proceedings of the 48th AIAA Joint Propulsion Conference, Atlanta, GA, 2012.

[8] J. M. Haas, R. R. Hofer, D. L. Brown, B. M. Reid and A. D. Gallimore, "Design of a 6kW Hall thruster for high thrust/power investigation", in 54th JANNAF Propulsion Meeting, Denver, Colorado, 2007.

[9] I. G. Mikellides, R. R. Hofer, I. Katz and D. M. Goebel, "The effectiveness of magnetic shielding in high-Isp Hall thrusters", AIAA Paper No. 2013-3885, in Proceedings of the 49th AIAA Joint Propulsion Conference, San Jose, CA, 2013.

[10] R. R. Hofer, B. A. Jorns, J. E. Polk, I. G. Mikellides and J. S. Snyder , "Wear test of a magnetically shielded Hall thruster at 3000 seconds specific impulse", IEPC Paper No. 2013-033, in Proceedings of the 33rd International Electric Propulsion Conference, Washington, DC, 2013

[11] I. G. Mikellides and A. Lopez Ortega, "Assessment of pole erosion in a mangetically shielded Hall thruster", AIAA Paper No. 14-3897, in Proceedings of the 50th AIAA Joint Propulsion Conference, Cleveland, Ohio, July, 2014..

[12] M. Sekerak, R. Hofer, J. Polk, B. Jorns and I. G. Mikellides, "Wear testing of a magnetically shielded Hall thruster at 2000s specific impulse", in Proceedings of the 34th International Electric Propulsion Conference, Kobe, Japan, July, 2015.

[13] R. P. Doerner, D. G. Whyte, and D. M. Goebel, "Sputtering yield measurements during low energy xenon plasma bombardment", Journal of Applied Physics, Vol. 93, No. 9, 2003, pp. 5816

[14] J. R. Gruber, "Low-energy sputter erosion of various materials in a T5 ion thruster", in proceedings of the 27th International Electric Propulsion Conference, Pasadena, CA, 2001

[15] D. Rosenberg and G. K. Wehner, "Sputtering yields for low energy He+, Kr+, and Xe+ ion bombardment", Journal of Applied Physics, Vol. 32, 1962, pp.1842

[16] R. D. Kolanski, J. E. Polk, D. M. Goebel, L. K. Johnson, "Sputtering yield measurements at glancing incidence using a quartz crystal microbalance", Journal of Vaccum Science and Technology A, Vol. 25, Issue 2, 2007, pp. 236

[17] R. Deltschew, M. Tartz, V. Plicht, E. Hartmann, H. Neumann, H.J. Leiter, J. Esch, "Sputter characteristics of carbon-carbon compound material", IEPC paper 2001-118, in proceedings of the 37th International Electric Propulsion Conference, Pasadena, CA, 2001

[18] J.D. Williams, M.L. Johnson, D.D. Williams, "Differential sputtering behavior of pyrolytic graphite and carbon–carbon composite under xenon bombardment, AIAA paper 2004-3788, in proceedings of the 40th AIAA Joint Propulsion Conference, Fort Lauderdale, Florida, July 2004.

[19] I. Katz and I. G. Mikellides, "Neutral gas free molecular flow algorithm including ionization and walls for use in plasma simulations", Journal of Computational Physics, Vol. 230, 2011, pp. 1454-1464

[20] A. Lopez Ortega and I. G. Mikellides, "A new cell-centered implicit numerical scheme for ions in the 2-D axisymmetric code Hall2De", AIAA paper 2014-3621, in proceedings of the 50th AIAA Joint Propulsion Laboratory, Cleveland, OH, 2014.

[21] R. Sullivan, "The physics of high-velocity ions in the Hall thruster near-field", Ph.D. thesis, California Institute of Technology, 2010

[22] G. D. Hobbs, and J. A. Wesson, "Heat Flow through a Langmuir Sheath in Presence of Electron Emission," *Plasma Physics,* vol. 9, no. 1, pp. 85-87, 1967.

[23] J. Bohdansky, J. Roth, and H. L. Bay, "An analytical formula and important parameters for low-energy ion sputtering", Journal of Applied Physics, Vol. 51, 1980, p. 2861.

[24] Y. Garnier, V. Viel, J. F. Roussel, and J. Bernard, "Low-energy xenon ion sputtering of ceramics investigated for stationary plasma thrusters", Journal of Vacuum Science and Technology A, Vol. 17, 1999, pp. 3246-3254

[25] Y. Yamamura and S. Shindo, "An empirical formula for angular dependence of sputtering yields", Radiation Effects, Vol. 80, 1984, pp. 52-72.

[26] A. Lopez Ortega and I. G. Mikellides, “The importance of the cathode plume and its interactions wit the ion beam in numerical simulations of Hall thrusters”, in proceedings of the 34th International Electric Propulsion Conference, Kobe, Japan, 2015.

[27] I. Katz, I. G. Mikellides, B. A. Jorns and A. Lopez Ortega, “Hall2De simulations with an anomalous transport model based on the electron drift instability”, IEPC paper 2015-402, in Proceedings of the 34th International Electric Propulsion Conference, Kobe, Japan, 2015.

[28] I. G. Mikellides, I. Katz, R. R. Hofer, and D. M. Goebel, “Hall-effect thruster simulations with 2-D electron transport and hydrodynamic ions”, IEPC paper 2009-114, in Proceedings of the 31st International Electric Propulsion Conference, Ann Arbor, Michigan, 2009.

[29] I. G. Mikellides, I. Katz, D. M. Goebel, J. E. Polk, and K. K. Jameson, “Evidence of non-classical plasma transport in hollow cathodes for electric propulsion”, Journal of Applied Physics, Vol. 101, No. 6, 2007, 063301

[30] I. G. Mikellides, D. M. Goebel, B. A. Jorns, J. E. Polk, and P. Guerrero, “Numerical simulations of the partially-ionized gas in a 100-A LaB6 hollow cathode”, IEPC paper 2013-142, in proceedings of the 33rd International Electric Propulsion Conference, Washington D.C., 2013.

[31] B. A. Jorns, I. G. Mikellides, and D. M. Goebel, “Ion acoustic turbulence in a 100-A LaB6 hollow cathode”, Physical Review E, Vol. 90, 2014, 063106.

[32] B.A. Jorns, I.G. Mikellides and D.M. Goebel, “Temporal fluctuations in a 100-A LaB6 hollow cathode”, IEPC Paper 2013-385, in Proceedings of the 33rd International Electric Propulsion Conference, Washington, DC, 2013

[33] R.Z. Sagdeev, A. Galeev, Nonlinear plasma theory, W. A. Benjamin, New York, 1969.

[34] B. A. Jorns, R. R. Hofer, and D. M. Goebel, "Study of Probe Perturbation Effects in the H6US”, Jet Propulsion Laboratory, California Institute of Technology, 2014, p. 52

[35] R. R. Hofer and J. R. Anderson, “Finite pressure effects in magnetically shielded Hall thrusters” AIAA paper 2014-3709, in proceedings of the 50th AIAA Joint Propulsion Conference, Cleveland, Ohio, 2014.

[36] D. M. Goebel, K. K. Jameson, I. Katz and I. G. Mikellides, “Energetic ion production and electrode erosion in hollow cathode discharges”, IEPC paper 05-269, in Proceedings of the 29th International Electric Propulsion Conference, Princeton, New Jersey, 2005.

[37] I. G. Mikellides and I. Katz, “Wear mechanisms in electron sources for ion propulsion I: neutralizer hollow cathode”, Journal of Propulsion and Power, Vol. 24, No. 4, 2008, 855-865

[38] I. G. Mikellides, I. Katz, D. M. Goebel, K. K. Jameson and J. E. Polk, “Wear mechanisms in electron sources for ion propulsion II: discharge hollow cathodes”, Journal of Propulsion of Power, Vol. 24, No 4, 2008, 866-879